Electronic Research Archive

ERA, 33(2): 768–790.
DOI: 10.3934/era.2025035
Received: 29 November 2024
Revised: 14 January 2025
Accepted: 17 January 2025
Published: 12 February 2025

https://www.aimspress.com/journal/ERA

Research article

Modeling and experimental investigation of quasi-zero stiffness vibration isolator using shape memory alloy springs

Xuerong Hu, Yuxiang Han, Junyan Lu and Linxiang Wang*

School of Mechanical Engineering, Zhejiang University, Hangzhou 310058, China

* **Correspondence:** Email: wanglx236@zju.edu.cn.

Abstract: Low-frequency vibration isolation is an attractive research topic in vibration control. In this study, a novel quasi-zero stiffness isolator utilizing shape memory alloy (SMA) springs is proposed. Leveraging the inherent stress plateau characteristics caused by the super-elastic effect of SMA, this design significantly improves the isolation performance at low-frequency excitations. We began by reformulating the static constitutive equation of the SMA spring, and the torsional strain of the spring was taken into account into the static constitutive equation. Subsequently, the dynamics of the SMA spring was modeled as an ordinary differential equation using the Euler-Lagrange equation. The SMA spring was fabricated and tensile tests were performed to validate the model given by dynamic differential function. Building on the validated spring model, a dynamic model of the quasi-zero stiffness isolator using SMA springs was proposed and its response under sinusoidal excitation was analyzed. The amplitude-frequency response of the system was determined using the harmonic balance method (HBM), and superior performance of the isolator in attenuating low-frequency vibrations was confirmed. Finally, an experimental platform was constructed to evaluate the isolator's performance under low-frequency excitations at 0.5, 1.0, 1.5, and 2.5 Hz. Our results demonstrated the effectiveness of the proposed quasi-zero stiffness vibration isolator system in isolating low-frequency vibrations, and the simulation results were verified by the experimental counterparts.

Keywords: quasi-zero stiffness; shape memory alloy spring; low-frequency vibration isolation; nonlinear system; analytical solution

1. Introduction

With the development of the engineering equipment, the detrimental effects of low-frequency vibrations have become more pronounced, leading to increasing interest in low-frequency vibration isolation technologies with a broader frequency ranges [1]. In passive vibration isolation technology, structures or materials with nonlinear stiffness are employed to lower the natural frequency while maintaining a high static load-bearing capacity, thereby achieving effective low-frequency isolation [2]. Among these methods, quasi-zero stiffness (QZS) isolation is a representative nonlinear low-frequency isolation technique, characterized by relatively low dynamic stiffness, which enables effective vibration isolation of low frequencies [3]. In practical applications, Li et al. [4] applied QZS isolators to a propulsion shaft system of underwater vehicles, providing a feasible method for effectively isolating longitudinal vibrations transferred from the propulsion shaft to the housing. Wu et al. [5] introduced a quasi-zero stiffness structure into a triboelectric vibration sensor (TVS), achieving a new level of ultra-wide frequency response and high sensitivity and offering insights for the development of high-resolution TVSs. Abuabiah et al. [6] used a QZS structure consisting of two oblique springs and a vertical spring in vehicle seats, resulting in a wider isolation frequency range for the seats.

The traditional QZS isolators are constructed by a parallel configuration of positive and negative stiffness structures [7–9]. Negative stiffness refers to the structural characteristic where the required force decreases as the displacement induced by a load increases. With advancements of quasi-zero stiffness theory, geometric nonlinear structures and novel nonlinear materials have been incorporated into quasi-zero stiffness isolators [10]. Geometric nonlinear structures leverage the unstable states and nonlinear dynamic responses of the structure to achieve negative stiffness [11–15]. Liu et al. [16] studied the nonlinear dynamic response of an origami systems and achieved quasi-zero stiffness vibration isolation. It was demonstrated that superior isolation performance of the designed isolator could be achieved, and the role of geometric nonlinearity effects has been illustrated by simulation studies. Yang et al. [17] established an analytical model for a 3D re-entrant honeycomb auxetic cellular structure, and the negative Poisson's ratio characteristics of the 3D honeycomb model was investigated. Fully recoverable negative stiffness honeycombs were fabricated using thermoplastic and metallic parent materials. It offers nearly ideal shock isolation performance and provides a new direction for the development of quasi-zero stiffness vibration isolators. Figure 1 illustrates three types of QZS structure. The emergence of magnetic negative stiffness technology also provides a new direction for achieving QZS vibration isolation [18]. By utilizing magnetic negative stiffness materials or devices, it is possible to achieve very low stiffness, effectively isolating low-frequency vibrations, especially in cases where traditional elastic isolation systems cannot meet the requirements [19]. Yang et al. [20] improved the vibration isolation performance of a semi-active suspension by integrating the negative stiffness mechanism with a magnetorheological (MR) damper. Zhu et al. [21] designed a novel six-degree-of-freedom vibration isolator using magnetic levitation as the payload support mechanism, which provides QZS in multiple directions and effectively enhances the vibration isolation performance.

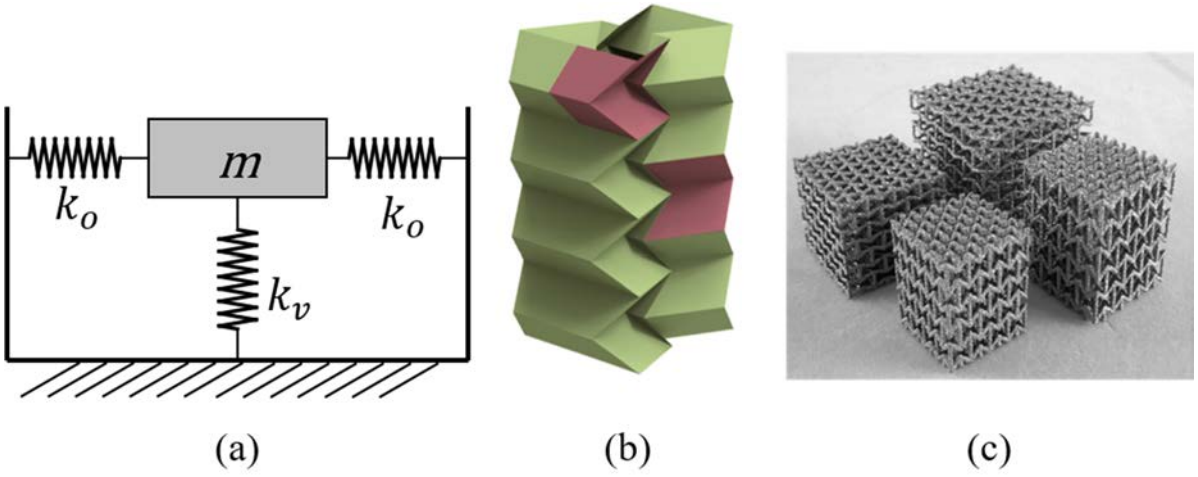


Figure 1. (a) The traditional QZS isolator [8], (b) origami QZS isolator [16], and (c) honeycomb structure used in vibration isolator [17].

Smart materials such as the shape memory alloy (SMA) exhibit inherent nonlinear stiffness, making them suitable for direct application in the construction of isolators. Moghadam et al. [22] verified the feasibility of using SMA for vibration isolation in their research. Rustighi et al. [23] implemented a tuned vibration absorber (TVA) using SMA. Du et al. [24] applied SMA in a vibration isolation model and conducted theoretical analysis. Song et al. [25] applied SMA to a civil structure, while Santos and Nunes [26] used real-time temperature modulation of SMA to control the elastic modulus of the elements, enabling continuous adjustment of stiffness over a wide frequency range.

SMA exhibits unique thermo-mechanical properties, enabling the conversion of mechanical energy into thermal energy and vice versa due to phase transformation. This distinctive, reversible change in physical properties could be induced under appropriate mechanical and thermal loads [27,28].

As illustrated in Figure 2, the stress-strain relationship of SMA reveals the phenomenon of a "stress plateau" [29]. Within this region, the dynamic stiffness of the SMA is exceptionally low, making it suitable for application in vibration isolation systems as a replacement for traditional linear elastic components. This characteristic, known as "super-elasticity" [30,31], is primarily caused by the phase transformation from austenite to martensite, which will induce significant strain to occur with minimal stress variation. However, this phenomenon is confined to a strain range. Outside of this range, SMA behaves similarly to conventional metals, undergoing elastic deformation in either the austenitic or martensitic phases [26,32,33]. For SMA-based vibration isolation systems, the high static stiffness ensures load-bearing capacity, while the low dynamic stiffness broadens the effective vibration-isolating range.

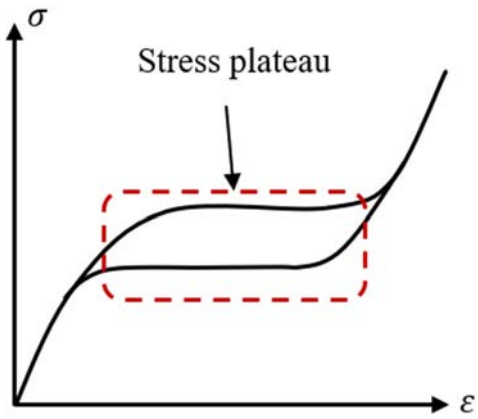


Figure 2. Stress plateau in SMA.

Here, we propose a quasi-zero stiffness vibration isolation system that primarily utilizes an external SMA springs accumulator as the main nonlinear component. The system will be referred to as SMAS-QZS. The system leverages the "stress plateau" caused by the phase transformation within SMA springs. The constitutive equations for the SMA spring are introduced, and a dynamic model for the SMAS-QZS is developed. Harmonic balance method is employed to derive analytical solutions for the amplitude-frequency response of the SMAS-QZS, and the analytical results are compared with those of a linear vibration isolation system to demonstrate the effectiveness of the quasi-zero stiffness system in isolating low-frequency vibrations. Finally, a prototype of SMAS-QZS for experimental purposes is setup and tested, and the amplitude-frequency response of the SMAS-QZS system under low-frequency sinusoidal displacement excitation is measured and compared with its theoretic counterparts. Both the accuracy of the simulation results and the effectiveness of the SMAS-QZS are verified.

2. Dynamic differential modeling of SMA spring

2.1. The constitutive function of SMA spring

In this paper, the Landau theory of phase transitions is utilized to describe the phase transformation of SMA spring [34,35]. According to the Landau theory, a fundamental characteristic of phase transitions is the change in symmetry. Typically, high-temperature phases exhibit greater symmetry of lattice structure, while specific symmetrical lattice structures are absent in low-temperature phases. Conversely, low-temperature phases display reduced symmetry, a phenomenon referred to as "symmetry loss", which arises due to the absence of certain symmetry structure present in high-temperature phase.

Changes in lattice structure symmetry reflect variations in the degree of order of the system, where a reduction in symmetry corresponds to an increase in order. The degree of order is quantified by a parameter known as order parameter, which is a fundamental parameter in characterizing the phase transition process. In high-symmetry phases, the order parameter is equal to zero, while in low-symmetry phases, it takes on a non-zero value.

Landau proposed that the free energy function of a system can be expressed as a power series

expansion in terms of the order parameter and temperature, retaining only the first few terms for practical applicability. The coefficients of the power series are determined based on the specific properties of the material. In this way, the phase transition process can be phenomenologically described through the free energy function. The essential part of modeling phase transition is to construct a free energy function where its minima represent the stable states of the material. Consequently, the phase transition process is characterized by the changes in the shape of the free energy function at different temperatures.

In this study, the Landau theory is applied to the SMA springs model, in which the Landau free energy function is constructed to model the transformation between the martensitic and austenitic phases. In the models proposed by Wang and Melnik [36], the strain ε is used as the order parameter to describe the phase transformation. The Landau free energy function is expressed as a function of the selected order parameter ε and temperature θ:

$$\Psi_{(\varepsilon,\theta)} = \frac{k_1(\theta-\theta_0)}{2}\varepsilon^2 + \frac{k_2}{4}\varepsilon^4 + \frac{k_3}{6}\varepsilon^6, \tag{1}$$

where, $\Psi_{(\varepsilon,\theta)}$ is the Landau free energy, k_1, k_2, and k_3 are basic material parameters, and θ_0 is the reference transformation temperature.

For SMA springs, the helical structure undergoes deformation under tensile and compressive loading. The axial force generates torque and shear stress on the cross-section of the spring. As a result, it is essential to consider the phase transformation of the SMA under torsional stress. In this paper, the conventional strain is replaced by torsional strain as the order parameter in the Landau free energy function. Consequently, Eq (1) is modified as shown in the following equation:

$$\Psi_{(\gamma,\theta)} = \frac{k_1(\theta-\theta_0)}{2}\gamma^2 + \frac{k_2}{4}\gamma^4 + \frac{k_2}{6}\gamma^6, \tag{2}$$

where γ is torsional strain.

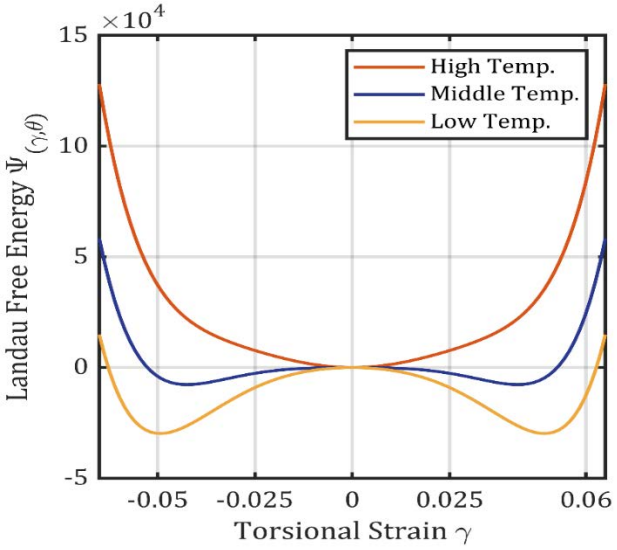


Figure 3. Landau free energy under different temperatures.

By plotting the free energy function with different temperatures, it is illustrated in Figure 3 that the free energy is strongly influenced by the material temperature [37]. It is evidenced that changes in SMA temperature induce phase transformations within the material. This is because, within a specific temperature range, certain phases lose stability and is transformed into other phases.

According to the constitutive relationship:

$$T = \frac{\partial \Psi}{\partial \gamma}. \tag{3}$$

Since the interest of the current investigation is about the hysteretic characteristics of the SMA spring as a whole, the distribution of torsional strain across the cross-section of the SMA spring is disregarded. In this context, the torsional strain is simplified to the torsional angle. The constitutive function can be expressed as follows:

$$T = k_1(\theta - \theta_0)\alpha + k_2\alpha^3 + k_3\alpha^5, \tag{4}$$

where T represents the torque, and α is the torsional angle. For simplicity, k_1, k_2, and k_3 are redefined parameters that incorporate basic material and geometric properties. To facilitate subsequent calculations of vibration isolation performance, it is necessary to convert the torsional angle into displacement, thereby establishing the force-displacement relationship for the SMA spring. When an external force F is applied, the spring undergoes a deformation x. The relationship between x and the torsional angle α, as well as the external force F and the torque T of the SMA wire, is expressed as:

$$T = FR,\ x = \alpha R, \tag{5}$$

where R is spring mean radius; thus, the constitutive function of SMA spring could be expressed as:

$$F = \frac{k_1(\theta-\theta_0)}{R^2}x + \frac{k_2}{R^4}x^3 + \frac{k_3}{R^6}x^5. \tag{6}$$

2.2. Dynamic differential model of SMA spring

In Section 2.1, the static constitutive equation for the SMA spring was derived. However, for the dynamic analysis of the vibration isolation system, it is essential to establish the dynamic model of the spring to accurately capture the hysteretic characteristics of the SMA spring. To achieve this, the Euler-Lagrange equation is employed to formulate the equation [38]. The general Euler-Lagrange equation is expressed as follows:

$$\frac{d}{dt}\left(\frac{\partial L}{\partial \dot{q}}\right) = \frac{\partial L}{\partial q}, \tag{7}$$

where L is the Lagrangian, q denotes the generalized coordinates, and $\dot{q}$ is generalized velocity. For a general physical system, the Lagrangian is typically defined as the difference between the kinetic energy and the potential energy, expressed as:

$$L = V - \Psi, \tag{8}$$

where V is the kinetic energy, and Ψ is the potential energy.

When the SMA spring is compressed, the system accumulates potential energy, which can be expressed as:

$$\Psi = \int_x^0 -F(x)dx. \tag{9}$$

Considering the phase transformation characteristics of the SMA spring, it is crucial to account for dissipative potential energy of the system. Therefore, a Rayleigh dissipative term is introduced, which is expressed as:

$$\mathbb{R} = -\frac{1}{2}\upsilon(\frac{dx}{dt})^2, \tag{10}$$

where υ is the dissipation parameter of the material.

Therefore, L can be expressed as:

$$L = \int_0^l (\frac{\rho}{2}(\dot{x})^2 - \Psi)dx, \tag{11}$$

where ρ represents the mass density of the material, x is the deformation of SMA spring, and $\frac{\rho}{2}(\dot{x})^2$ is the kinetic energy density of the system.

Substituting the potential energy Ψ and the dissipative term $\mathbb{R}$ into the Lagrange equation, the dynamic equation of the SMA spring is expressed as:

$$\frac{d^2x}{dt^2} + \nu\frac{dx}{dt} = A_1(\theta - \theta_0)x + A_2x^3 + A_3x^5 + f(t). \tag{12}$$

To facilitate subsequent expressions, A_1, A_2, and A_3 are newly defined parameters that encompass material and geometric properties, and $f(t)$ is the external force. In this study, the inertial term has a negligible effect on the system compared to the dissipative term [39], so that Eq (12) can be simplified as:

$$\nu\dot{x} - (A_1(\theta - \theta_0)x + A_2x^3 + A_3x^5) = f(t). \tag{13}$$

For further calculation, the parameters A_1, A_2, and A_3 need to be obtained by experimental measurement, and two types of SMA wires with different diameters were selected for the purpose. Due to experimental limitations, only SMA tension springs were fabricated. The SMA wire was wound around a screw rod and secured with clamps after winding. The assembly was then placed in a furnace and heated to 773.15 K for one hour. When it was cooled in air, the formed SMA spring was extracted from the screw rod. The SMA spring prepared for this study is shown in Figure 4. The parameters of SMA spring are shown in Table 1.

Table 1. Parameters of two types of SMA springs.

The Parameter of SMA spring (NiTi alloy)	1.0 mm wire SMA spring	1.5 mm wire SMA spring
Wire diameter (mm)	1	1.5
Mean diameter (mm)	7.5	8.2
Effective number of turns	30	30
Austenite phase transformation completely temperature (K)	258	258

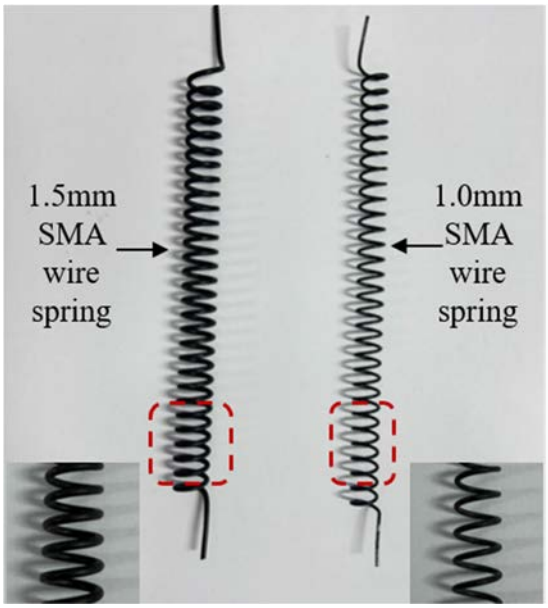


Figure 4. Two types of SMA springs.

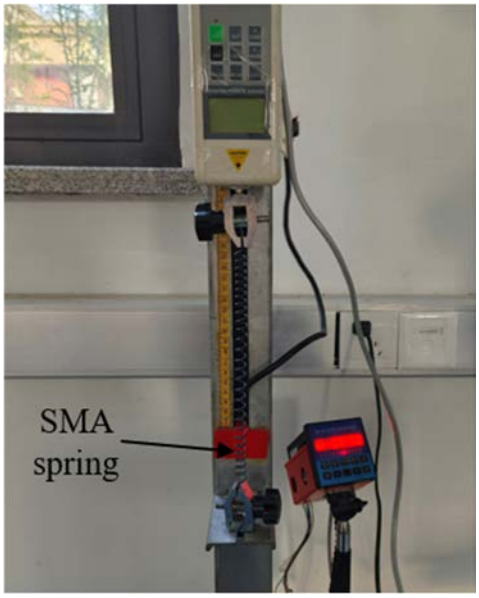


Figure 5. Cyclic tension test.

For newly formed SMA springs, it is crucial to perform multiple cycles of tensile training until the stimulation-response behavior of the spring reaches a stable state before proceeding with further analysis [29]. During each tensile cycle, it must be ensured that the SMA spring is transformed from the austenitic phase to the martensitic phase during the loading process and that it reverts back to the austenitic phase during the unloading process. As illustrated in Figure 5, one end of the spring is fixed to the frame, while the other end is attached to a force gauge. The force gauge is driven by a stepper motor to enforce cyclic tensile loading. A total of 25 loading cycles of training were performed.

It is shown in Figure 6 that both types of SMA springs exhibit significant hysteresis behavior, and the temperature is 285 K. As the number of cycles increases, the residual strain of the SMA springs continues to grow. However, after a certain number of cyclic trainings, the residual strain stabilizes, and the hysteresis loop for each cycle becomes nearly identical. This indicates that the training process of the SMA spring is completed, and the measured stimulation-response curve is appropriate for parameter identification and further analysis. For clarification purposes, the experimental tension-deformation curve with hysteresis loop of the final cycle is presented in Figure 6 by thick solid lines.

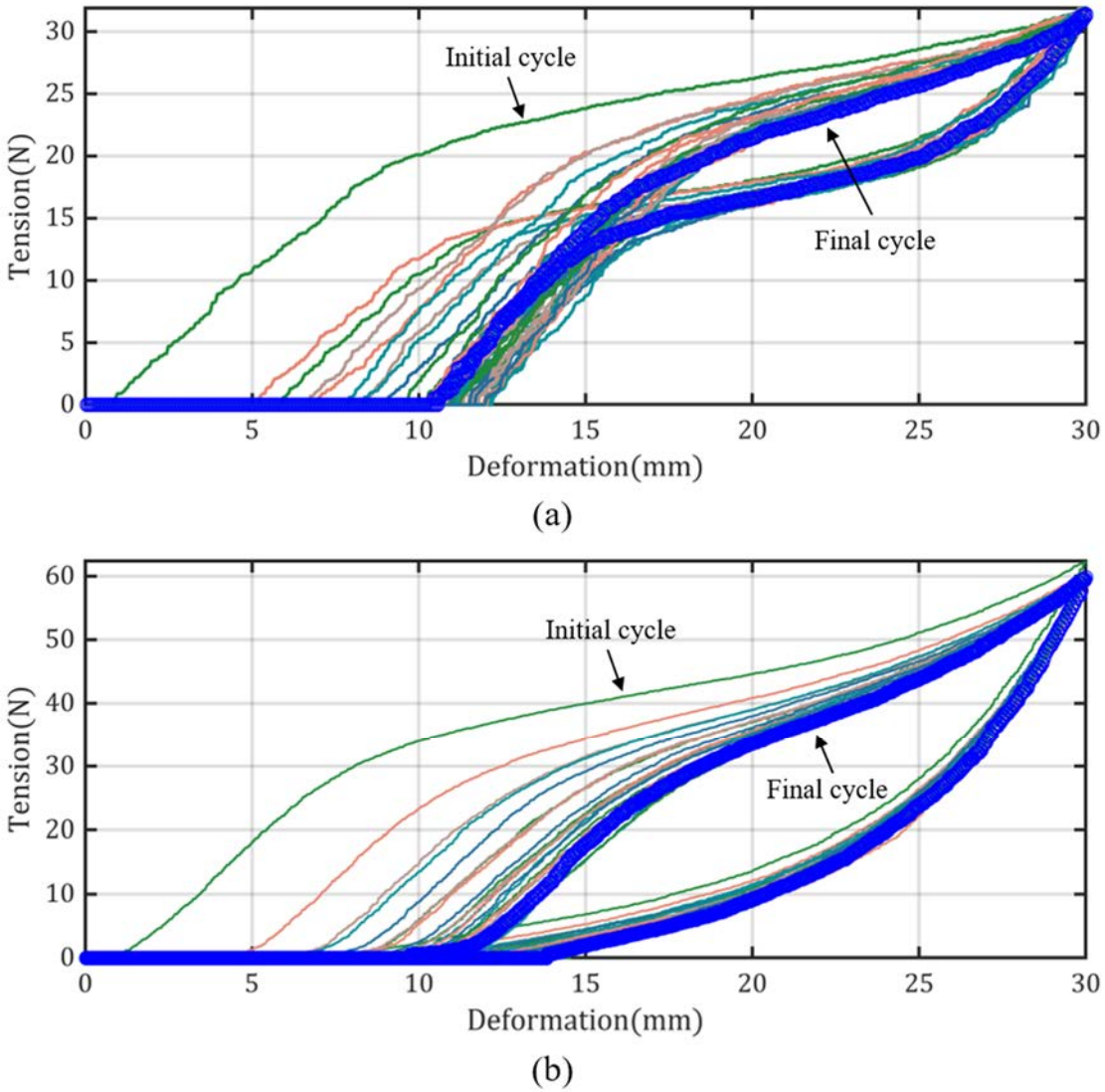


Figure 6. Cyclic loading of SMA springs. (a) 1.0 mm SMA wire and (b) 1.5 mm SMA wire.

2.3. Parameter identification

In order to estimate the model parameters, the final cycle of the tensile training process for both sets of springs are taken for parameter identification purposes. Concerning the numerical stability of the hysteretic dynamics, the mentioned constitutive model is approximated by a lower piecewise polynomial instead of a high order polynomial. Moreover, the nonlinear least square approximation method is employed to estimate the parameters in the model, aiming to minimize the discrepancy between the simulated values and the experimental data. Consequently, the parameter identification problem is reformulated as a nonlinear optimization problem, expressed by the following equation:

$$\min_{p,q,n,v} G = \sum_{i=1}^{M} (\widetilde{C}_i - C_i)^2, \tag{14}$$

where $p, q,$ and n represent the values on the y-axis at the interpolation points, v is the time constant,

M is the number of selected experimental data points, $\widetilde{C_i}$ denotes the displacement value corresponding to the i-th data point from the experimental results, and C_i is the simulated displacement. To achieve precise identification of the four parameters simultaneously, the Nelder-Mead nonlinear optimization algorithm is employed and implemented using the MATLAB's built-in *fminsearch* function [40].

For the 1.0 mm wire SMA spring, the coordinates of the interpolation points are: (0,0), (12.03,p), (13.91,q), and (19.60,n). For the 1.5 mm wire SMA spring, the coordinates of interpolation points are: (0,0), (7.92,p), (11.74,q), and (18.90,n). $p, q,$ and n are the y-coordinates of these interpolation points. Those points are marked in Figure 7, where p indicates the beginning of the transformation of austenite to martensite within the SMA spring, n represents the end of the transformation, and q indicates the reverse process.

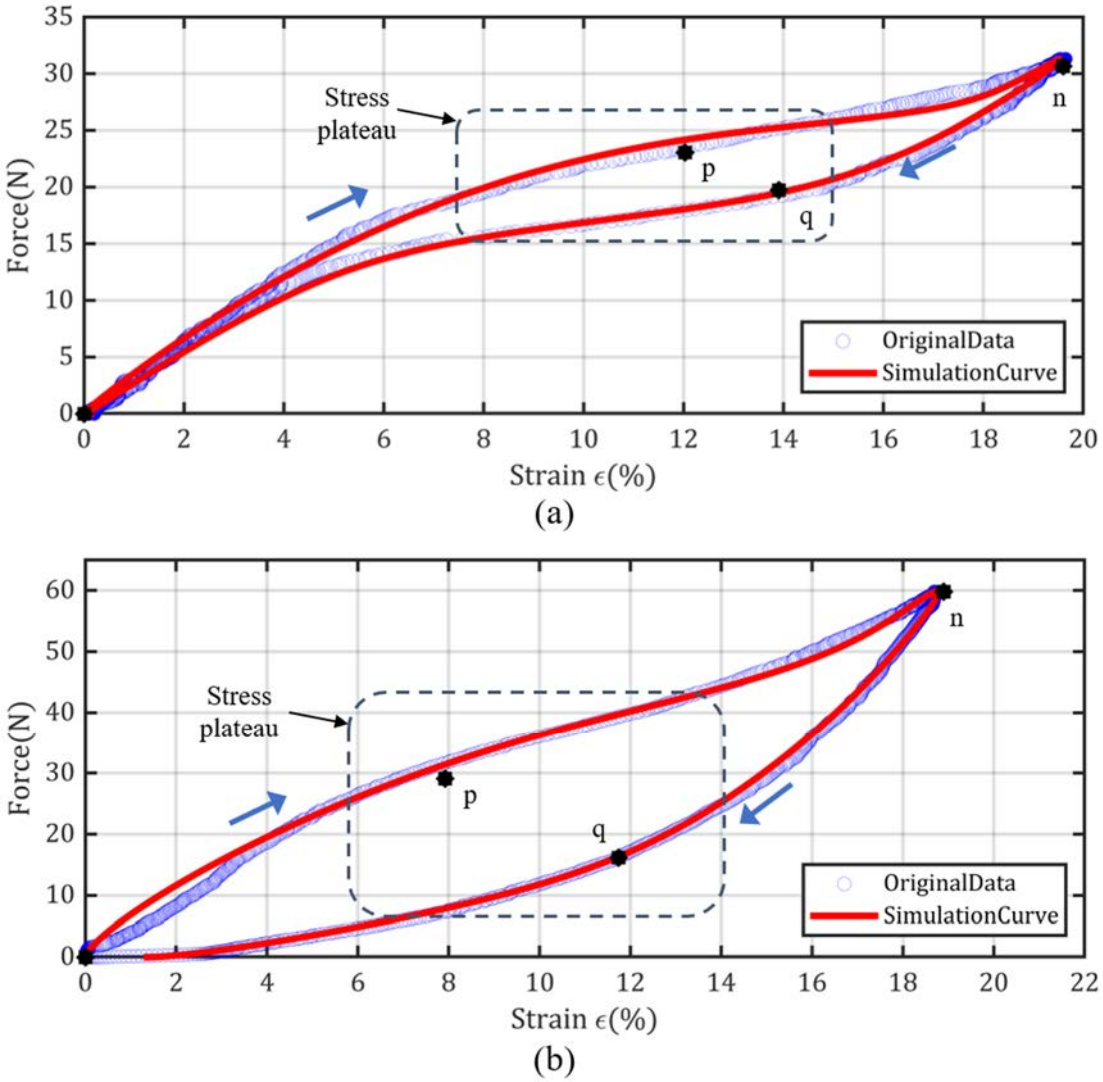


Figure 7. The result of parameter identification: (a) 1.0 mm wire SMA spring and (b) 1.5 mm wire SMA spring.

In Figure 7, the experimental values and simulated values are compared. It can be observed that the constitutive model, given as the differential equation, effectively captures the super-elasticity effect of the SMA spring and accurately predicts the forces at various states during the tensile cycles. The results of the parameter identification based on the experimental data are presented in Table 2 and 3. From Figure 7, it is evident that the hysteresis phenomenon in the 1.5 mm wire SMA spring is particularly pronounced. The upper plateau demonstrates a strong load-bearing capacity, while the lower plateau could support a smaller load, with a less distinct stress plateau effect. In contrast, the 1.0 mm wire SMA spring exhibits a more distinct stress plateau phenomenon, and the distance between the upper and lower plateau of the hysteresis loop is smaller; this characteristic makes it more suitable for use in the SMAS-QZS vibration isolator system. Therefore, the 1.0 mm wire SMA spring is selected for vibration isolation.

Table 2. Parameters identified of 1.0 mm wire SMA spring.

	v	p	q	n
Initial value	0.01	23.60	19.72	30.65
Optimized value	0.22	21.50	21.68	31.41

Table 3. Parameters identified for the 1.5 mm wire SMA spring.

	v	p	q	n
Initial value	0.01	29.1	16.16	59.8
Optimized value	0.157	22.615	19.354	58.650

3. Analysis of the vibration isolation characteristics of SMAS-QZS

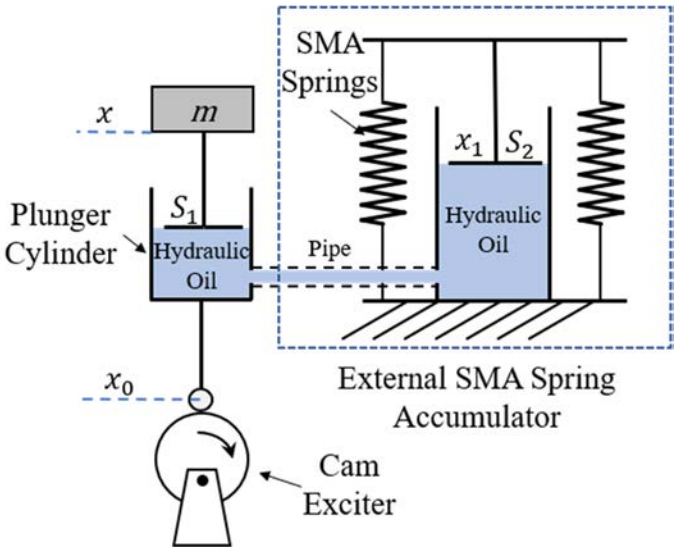


Figure 8. The model of the proposed SMAS-QZS vibration isolator.

Due to fabrication constraints, only tension springs were fabricated, which differ from linear

compression springs commonly used in traditional passive vibration isolation systems. To integrate the tension springs into a quasi-zero stiffness system, the SMA springs are installed within an external accumulator, as shown in Figure 8. The function of the accumulator is to provide displacement compensation for the plunger and ensure adequate load-bearing capacity. It consists of a plunger cylinder and several SMA springs. The accumulator is connected via a tube to a plunger, and a mass block m is mounted on top of the plunger. One end of each spring is fixed to the frame and the other end is attached to the plunger. These springs generate both static supporting force and dynamic force, and the force is transmitted to the mass block m through hydraulic oil. A cam exciter is installed beneath the plunger to provide sinusoidal displacement excitation. To enhance the quasi-zero stiffness characteristics of the system, the springs are pre-stretched into the stress plateau range, as illustrated in the range marked in Figure 7(a).

The dynamic equation for the mass block can be expressed as follows:

$$m\ddot{x} + F_C = F_{QZS}, \tag{15}$$

where x is the displacement of the mass, F_C denotes the system damping force, and F_{QZS} is the force provided by the external SMA springs accumulator through the hydraulic oil. Due to the difference in cross-sectional areas of the plunger and the accumulator, the displacements of the mass block and the SMA springs are not identical, and the equation can be written as follows:

$$\begin{gathered} (x_0 - x)S_1 = x_1 S_2 \\ \frac{F_{QZS}}{S_1} = \frac{F_{SMA}}{S_2} \\ F_{SMA} = n(v\dot{x_1} - A_1(\theta - \theta_0)x_1 - A_2{x_1}^3 - A_3{x_1}^5) \\ F_C = c(\dot{x} - \dot{x_0}) \end{gathered}, \tag{16}$$

where x_0 is the sinusoidal displacement excitation, ω is the excitation frequency, x_1 denotes the displacement of the plunger in accumulator and also the displacement of the SMA springs, F_{SMA} is the force of SMA springs, S_1 and S_2 are the cross-sectional areas of the plunger and the accumulator separately, n is the number of SMA springs, and c is the system damping coefficient, which is taken from reference [36]. By substituting Eq (16) into Eq (15), the dynamic equation can be rewritten as:

$$\begin{gathered} m\ddot{x} + c(\dot{x} - \dot{x_0}) = \\ nS\left[vS(\dot{x_0} - \dot{x}) - A_1(\theta - \theta_0)S(x_0 - x) - A_2S^3(x_0 - x)^3 - A_3S^5(x_0 - x)^5\right] \end{gathered}, \tag{17}$$

where $S = S_1/S_2$. To simplify the process of calculation, the relative displacement $y = x - x_0$ is substituted into Eq (17):

$$\ddot{y} + C\dot{y} + a_1(\theta - \theta_0)y + a_2y^3 + a_3y^5 = \ddot{x_0}, \tag{18}$$

where $C = \frac{nvS^2 + c}{m}$, $a_1 = -\frac{nS^2A_1}{m}$, $a_2 = -\frac{nS^4A_2}{m}$, and $a_3 = -\frac{nS^6A_3}{m}$.

The excitation part of the model is an eccentric cam structure. The cam is designed as a cylinder with a radius of $r_2 = 28$ mm, featuring an eccentric hole with a distance of $d = 10$ mm. The top surface of the cam is in contact with a roller, which has a radius of $r_1 = 6.5$ mm. The motion trajectory

is illustrated in Figure 9.

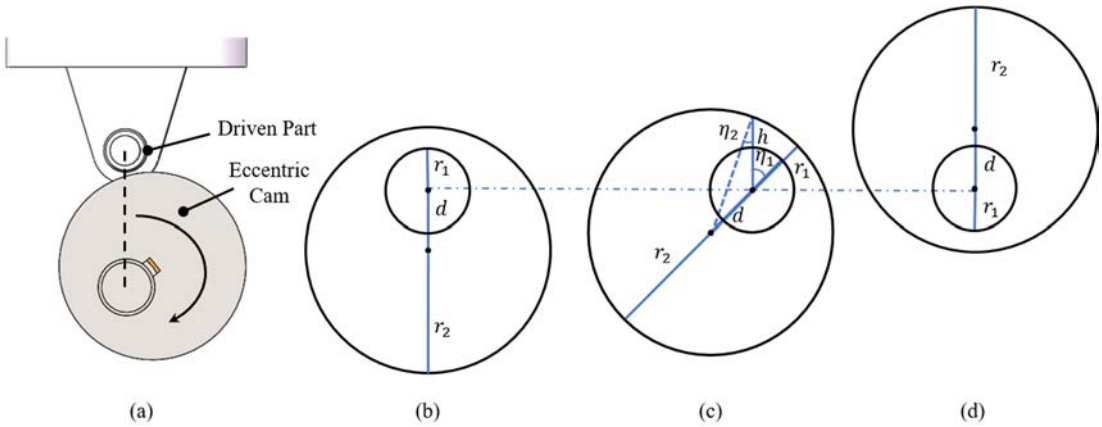


Figure 9. Geometric analysis of the cam: (a) Cam and driven part, (b) low position, (c) random position, and (d) high position.

According to the sine theorem, the relationship between those geometrical parameters of the cam can be expressed as follows:

$$\frac{r_2}{sin(\pi-\eta_1)} = \frac{d}{sin\,\eta_2} = \frac{h}{sin(\eta_1-\eta_2)}, sin\,\eta_2 = \frac{d}{r_2} sin\,\eta_1. \tag{19}$$

The displacement of the excitation can be expressed as follows (set the initial height as 0):

$$h = \sqrt{{r_2}^2 - (d\,sin\,\eta_1)^2} - dcos\,\eta_1 - (r_2 - \mathrm{d}). \tag{20}$$

As illustrated in Figure 10, the excitation curve fits the theoretical sinusoidal curve.

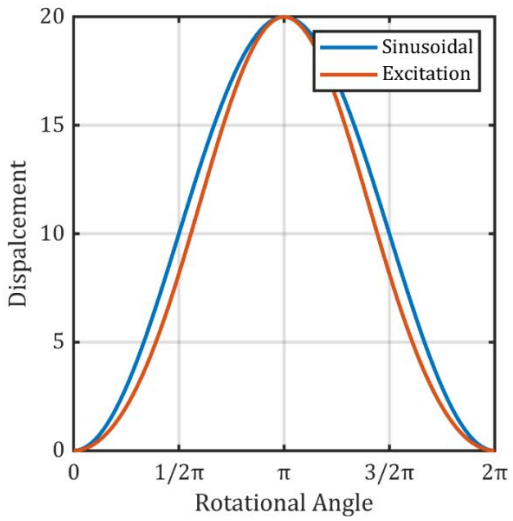


Figure 10. Excitation curve.

Therefore, the sinusoidal displacement excitation can be represented as: $x_0 = x_m \cos(\omega t)$, and x_m is the amplitude of excitation.

The HBM [41] is used to obtain analytical solution of Eq (18). The solution of the function is expanded into Fourier series as follows:

$$y = y_0 + \sum_{n=1}^{N}[\alpha_n \cos(n\omega_0 t) + \beta_n \sin(n\omega_0 t)]. \tag{21}$$

The system starts from the static state, so $y_0 = 0$. The HBM considers only the first-order harmonic approximation and neglects the higher-order harmonic. It is assumed that the relative displacement y shares the same frequency as the external excitation:

$$y = \alpha \cos(\omega t) + \beta \sin(\omega t). \tag{22}$$

Substitute Eq (22) into Eq (18) and make the coefficients of the $\sin(\omega t)$ and $\cos(\omega t)$ terms on either side of the equation equal:

$$\begin{aligned} -\omega^2\alpha + C\omega\beta + a_1(\theta - \theta_0)\alpha + \frac{3}{4}a_2(\alpha^2 + \beta^2)\alpha + \frac{5}{8}a_3(\alpha^2 + \beta^2)^2\alpha = -\omega^2 x_m \\ -\omega^2\beta - C\omega\alpha + a_1(\theta - \theta_0)\beta + \frac{3}{4}a_2(\alpha^2 + \beta^2)\beta + \frac{5}{8}a_3(\alpha^2 + \beta^2)^2\beta = 0 \end{aligned}. \tag{23}$$

The value of response amplitude $Y = \sqrt{\alpha^2 + \beta^2}$ is calculated by Eq (23):

$$Y = \sqrt{\frac{\omega^4 {x_m}^2}{(-\omega^2 + a_1(\theta - \theta_0) + \frac{3}{4}a_2 Y^2 + \frac{5}{8}a_3 Y^4)^2 + C^2\omega^2}}. \tag{24}$$

The response amplitude of the model is represented in a non-dimensional displacement form:

$$X = \frac{x}{x_m}. \tag{25}$$

To better evaluate the performance of the SMAS-QZS in isolating low-frequency vibrations, a damped linear vibration isolation system is introduced for comparison. The linear system utilizes the same damping value and an appropriate stiffness. The calculation process of the linear system is not elaborated here, and the result is presented as follows:

$$X_{linear} = \frac{x_{linear}}{x_m} = \frac{1}{\sqrt{(1 - r_\omega^2)^2 + (2\xi r_\omega)^2}}, \tag{26}$$

where r_ω is the frequency ratio, and ξ denotes the damping ratio.

As illustrated in Figure 11, compared to the linear system, the response amplitude curve of SMAS-QZS exhibits strong nonlinear characteristics. Due to the inherent stress plateau characteristics of the SMA spring, the natural frequency of the system is significantly reduced. A lower natural frequency of system could effectively broaden the vibration isolation frequency range, especially the low-frequency. Therefore, the SMAS-QZS could effectively isolate the low-frequency vibration.

Additionally, the phase transition between austenite and martensite within SMA during the stretching process dissipates vibration energy and contributes to amplitude suppression. The reference temperature is $\theta_0 = 208K$,and the values of the parameters are: $a_1 = 229.8, a_2 = -1.8 \times 10^3, a_3 = 1.5 \times 10^6,$ and $C = 70$.

In Figure 11(a), due to the nonlinear characteristics of the system, the response amplitude exhibits multiple solutions within a certain region; thus, the system is unstable within this region. The impact of different damping ratios on the response amplitude of the system is illustrated in Figure 11(b). As the damping ratio increases, the response amplitude decreases.

In order to validate the influence of temperature on the isolation performance of SMAS-QZS, the response amplitude at different temperatures is compared. As illustrated in Figure 12, it can be observed that as the temperature increases, the degree of nonlinearity in the system decreases. When the temperature exceeds a certain threshold, the characteristics of response amplitude become nearly identical to those of a linear system. This is because the austenite in the material at high temperatures cannot transform into martensite under the stress, and the stress plateau characteristics disappear as a result [29]. Consequently, the quasi-zero stiffness characteristics of the SMAS-QZS nearly vanishes at high temperature.

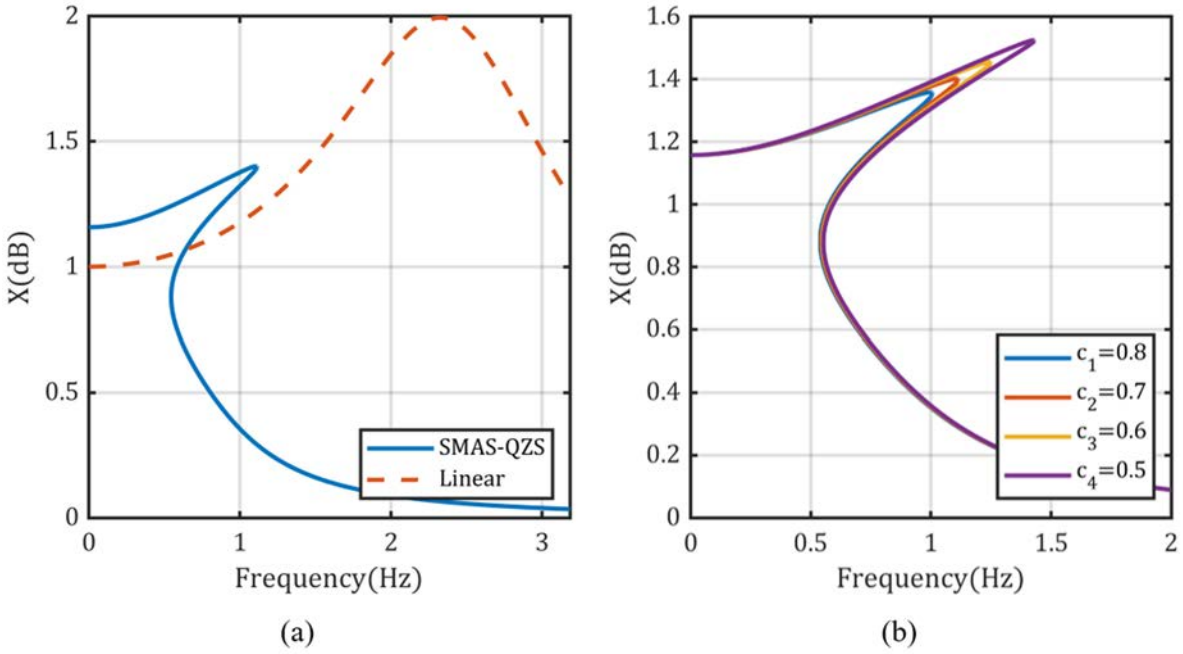


Figure 11. The response amplitude: (a) Comparison with the linear system, and (b) comparison with different damping ratios.

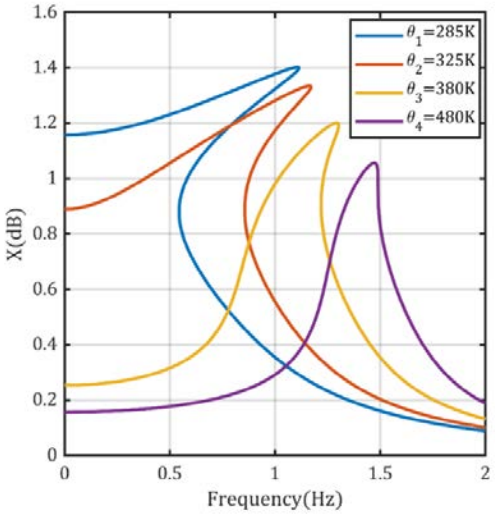


Figure 12. The response amplitude at different temperatures.

4. Experiment verification

4.1. SMAS-QZS experiment system

To validate the accuracy of the simulation results, an experimental system is established. The theoretical structure of the experimental system is illustrated in Figure 13.

The excitation component is illustrated in Figure 14 and consists of a stepper motor and a cam mechanism. The motor is controlled by the Arduino microcontroller and provides the rotational motion in different frequencies for the cam mechanism. The cam mechanism converts the rotational motion of the motor into a sinusoidal displacement excitation.

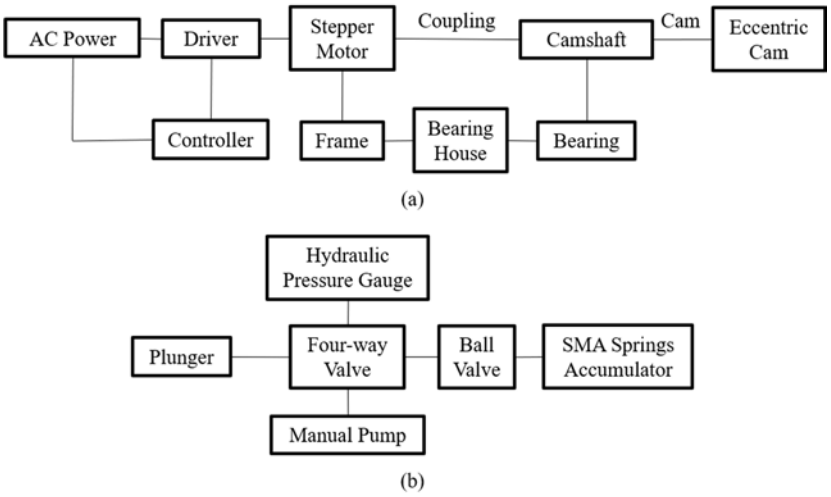


Figure 13. Theoretical structure of the experimental system: (a) Excitation component, and (b) hydraulic component.

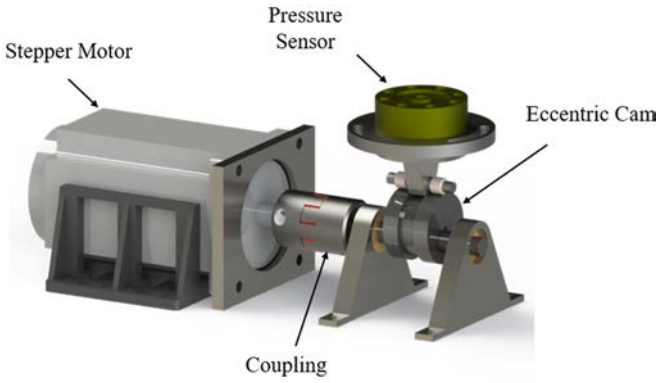


Figure 14. Excitation component.

The SMA springs accumulator proposed in this study is illustrated in Figure 15(a). It leverages the stress plateau characteristics of SMA to achieve quasi-zero stiffness characteristics. Due to the limitation of using only tension SMA springs, an experimental design is developed. The SMA springs accumulator mostly consists of a plunger and several SMA springs. The plunger within the accumulator is connected to the load-bearing plunger cylinder via a pipe to enable force transmission.

The force comes from a certain number of SMA springs arranged circumferentially around the plunger cylinder. The number of SMA springs can be adjusted to 2, 4, 6, or 8 depending on the load weight. To ensure the piston moves only vertically, an external guiding mechanism is incorporated consisting of sliders and shafts. As shown in Figure 15(b), sliders and shafts are utilized to ensure the load-bearing platform moves only in the vertical direction.

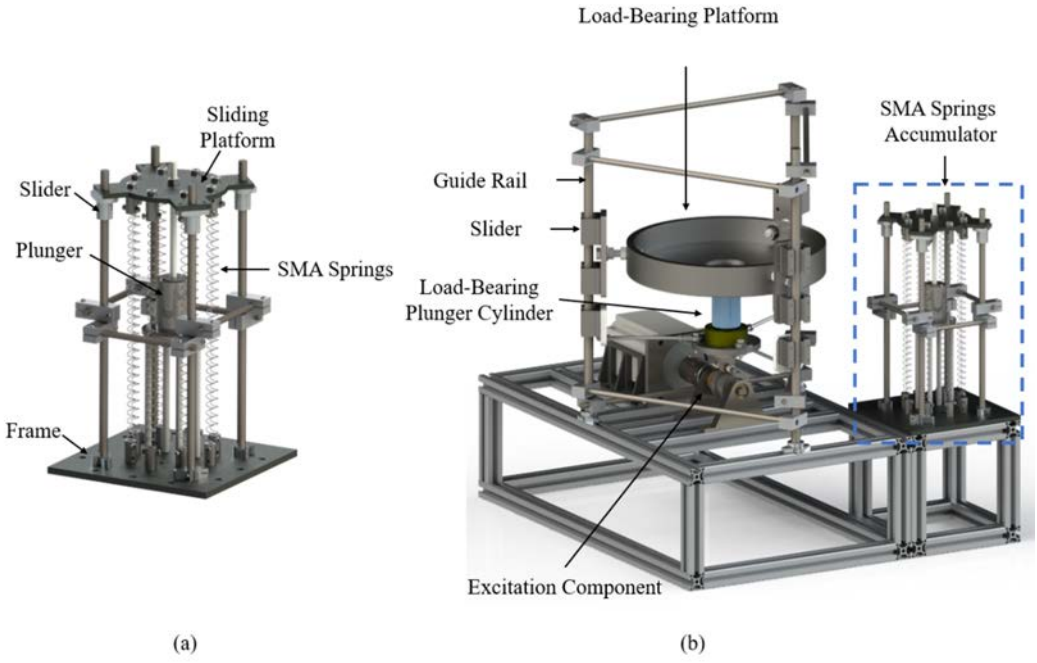


Figure 15. (a) SMA springs accumulator, and (b) SMAS-QZS experimental model.

A retractable displacement sensor is mounted with one end fixed to the frame and the other end attached to the load-bearing platform, measuring the response displacement of the platform during the experimental process. All sensor signals are processed through an amplifier before being transmitted to a data acquisition card, ensuring the accuracy and reliability of the data. The experiment setup and prototype of SMAS-QZS is shown in Figure 16.

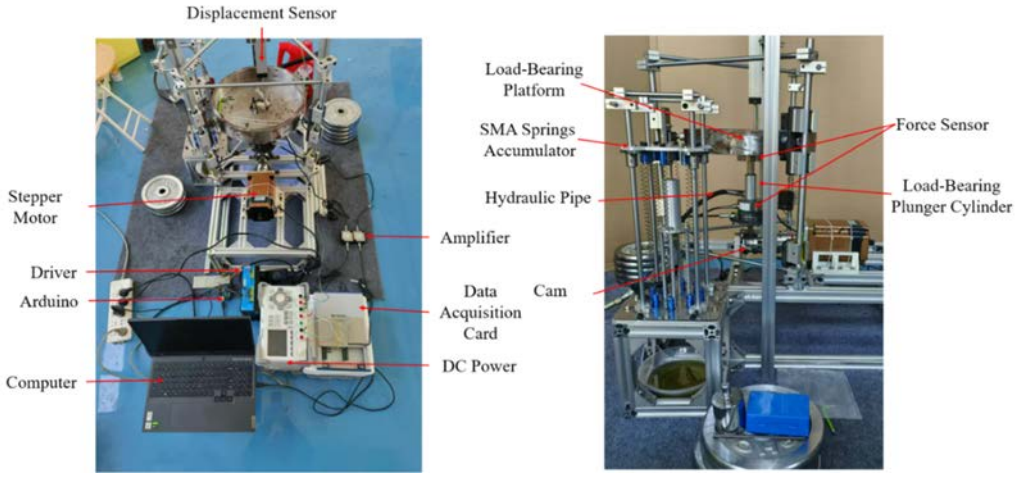


Figure 16. SMAS-QZS experiment system.

4.2. Experiment results

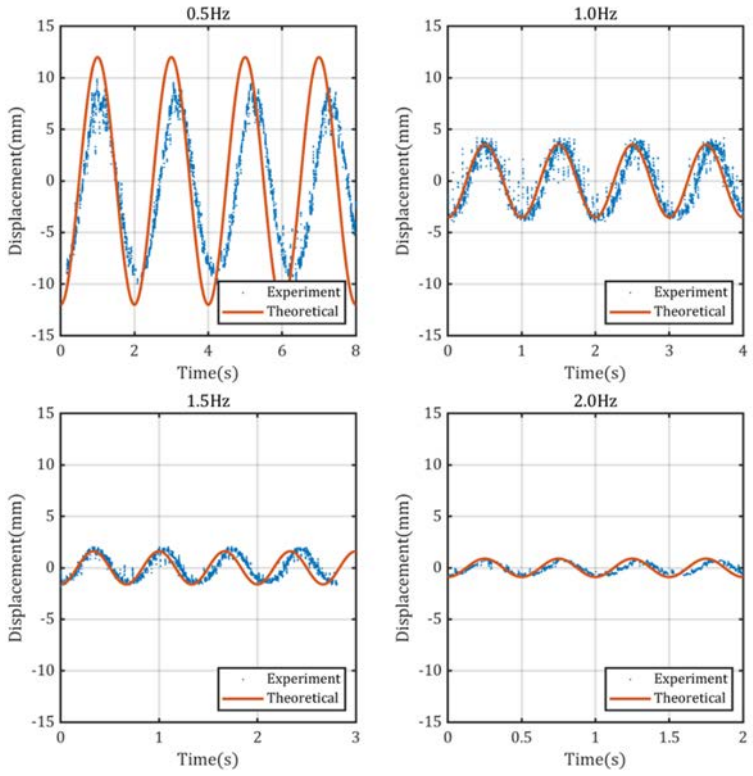


Figure 17. Response displacement at different frequencies.

The response displacement and simulation results of SMAS-QZS at 0.5, 1.0, 1.5, and 2.0 Hz are illustrated in Figure 17; the data is processed using filters to remove noise signals. Due to the output error of the motor, there is a certain phase difference between the experimental data and the simulation results. From Figure 17, it can be observed that experimental response displacement aligns well with the simulation results across excitation frequencies.

As illustrated in Figure 17, the response displacement exceeds the amplitude of the excitation at an input frequency of 0.5 Hz. This is because 0.5 Hz is within the resonance region, and the system is unable to isolate vibrations at this frequency. At frequencies above 1.0 Hz, the vibration isolation capability of the system is significantly enhanced, and the vibration suppression effect for the excitation displacement reaches over 50%. This phenomenon verifies the accuracy of the displacement response simulation results. When the excitation frequency exceeds 0.5 Hz, it surpasses the natural frequency of the system. Therefore, the resonance phenomenon disappears, and the vibration isolation capability of the system becomes apparent. Consequently, the system effectively isolates vibrations with the frequency above 0.5 Hz, and the effectiveness of the system in isolating low-frequency vibrations also demonstrates the quasi-zero stiffness characteristic.

5. Conclusions

In this paper, a novel quasi-zero stiffness vibration isolation model using SMA springs is proposed. First, the Landau theory is utilized to construct the static constitutive equation of the SMA spring. The static constitutive equation can describe the characteristics of the phase transformation from austenite to martensite. Subsequently, the Euler-Lagrange equation is utilized to develop the dynamic model.

To obtain the parameters of the dynamic model, tensile tests are conducted on SMA springs with different wire diameters to obtain the force-displacement characteristics, and the parameters are identified using the nonlinear least square optimization method. To effectively leverage the stress plateau characteristics of the SMA spring, an external SMA springs accumulator is employed to develop a theoretical quasi-zero stiffness vibration isolation model (SMAS-QZS), and the SMA springs are pre-stretched to a specific length. The HBM is used to derive an analytical solution for the amplitude-frequency response. The analytical results are compared with those of a linear vibration isolation system to demonstrate the effectiveness of the quasi-zero stiffness system in isolating low-frequency vibrations. Furthermore, we examine the effects of different parameters on the vibration isolation performance of SMAS-QZS, such as damping ratio and temperature.

Finally, a prototype of SMAS-QZS for the experimental purpose is set up and tested, and the amplitude frequency response of the experimental system under low-frequency sinusoidal displacement excitation is measured and compared with its theoretic counterparts. By applying external excitations within the frequency range of 0.5–2.0 Hz, the experimental data aligns well with the simulation results. The system is proven to effectively isolate vibrations at frequencies above 0.5 Hz.

Use of AI tools declaration

The authors declare they have not used Artificial Intelligence (AI) tools in the creation of this article.

Acknowledgments

This work has been supported by the National Natural Science Foundation of China (Grant Nos. 51575478 and 61571007).

Conflict of interest

The authors declare there is no conflict of interest.

References

1. B. Yan, N. Yu, C. Wu, A state-of-the-art review on low-frequency nonlinear vibration isolation with electromagnetic mechanisms, *Appl. Math. Mech.*, **43** (2022), 1045–1062. https://doi.org/10.1007/s10483-022-2868-5
2. L. Guo, X. Wang, R. Fan, F. Bi, Review on development of high-static–low-dynamic-stiffness seat cushion mattress for vibration control of seating suspension system, *Appl. Sci.*, **10** (2020), 2887. https://doi.org/10.3390/app10082887
3. Z. Ma, R. Zhou, Q. Yang, Recent advances in quasi-zero stiffness vibration isolation systems: An overview and future possibilities, *Machines*, **10** (2022), 813–854. https://doi.org/10.3390/machines10090813
4. X. Li, S. Huang, Y. Xu, J. Liu, J. Liu, G. Pan, Dynamic analysis of a quasi-zero stiffness vibration isolator in propulsion shaft system, *Ocean. Eng.*, **313** (2024), 119544–119560. https://doi.org/10.1016/j.oceaneng.2024.119544
5. P. Wu, F. Wang, S. Xu, T. Liu, Y. Qi, X. Zhao, et al., A highly sensitive triboelectric quasi-zero stiffness vibration sensor with ultrawide frequency response, *Adv. Sci.*, **10** (2023), 2301199–2301209. https://doi.org/10.1002/advs.202301199
6. M. Abuabiah, Y. Dabbas, L. Herzallah, I. H. Alsurakji, M. Assad, P. Plapper, Analytical study on the low-frequency vibrations isolation system for vehicle's seats using quasi-zero-stiffness isolator, *Appl. Sci.*, **12** (2022), 2418–2436. https://doi.org/10.3390/app12052418
7. C. Liu, W. Zhang, K. Yu, T. Liu, Y. Zheng, Quasi-zero-stiffness vibration isolation: Designs, improvements and applications, *Eng. Struct.*, **301** (2024), 117282–117307. https://doi.org/10.1016/j.engstruct.2023.117282
8. Y. Chang, J. Zhou, K. Wang, D. Xu, A quasi-zero-stiffness dynamic vibration absorber, *J. Sound Vib.*, **494** (2021), 115859–115868. https://doi.org/10.1016/j.jsv.2020.115859
9. P. Alabuzhev, *Vibration Protection and Measuring Systems with Quasi-zero Stiffness*, CRC Press, 1989.
10. J. C. Ji, Q. Luo, K. Ye, Vibration control based metamaterials and origami structures: A state-of-the-art review, *Mech. Syst. Signal Process.*, **161** (2021), 107945–107983. https://doi.org/10.1016/j.ymssp.2021.107945
11. H. Han, V. Sorokin, L. Tang, D. Cao, A nonlinear vibration isolator with quasi-zero-stiffness inspired by Miura-origami tube, *Nonlinear Dyn.*, **105** (2021), 1313–1325. https://doi.org/10.1007/s11071-021-06650-6

12. D. Wang, Q. Zhang, G. Hu, Low frequency waterborne sound insulation based on sandwich panels with quasi-zero-stiffness truss core, *J. Appl. Mech.*, **90** (2023), 031066–031074. https://doi.org/10.1115/1.4056316
13. L. Wang, Y. Zhao, T. Sang, H. Zhou, P. Wang, C. Zhao, Ultra-low frequency vibration control of urban rail transit: The general quasi-zero-stiffness vibration isolator, *Veh. Syst. Dyn.*, **60** (2021), 1788–1805. https://doi.org/10.1080/00423114.2021.1874428
14. N. A. Kamaruzaman, W. S. P. Robertson, M. H. Ghayesh, B. S. Cazzolato, A. C. Zander, Six degree of freedom quasi-zero stiffness magnetic spring with active control: Theoretical analysis of passive versus active stability for vibration isolation, *J. Sound Vib.*, **502** (2021), 116086–116106. https://doi.org/10.1016/j.jsv.2021.116086
15. K. Ye, J. C. Ji, An origami inspired quasi-zero stiffness vibration isolator using a novel truss-spring based stack miura-ori structure, *Mech. Syst. Signal Process.*, **165** (2022), 108383–108396. https://doi.org/10.1016/j.ymssp.2021.108383
16. S. Liu, G. Peng, K. Jin, Towards accurate modeling of the tachi-miura origami in vibration isolation platform with geometric nonlinear stiffness and damping, *Appl. Math. Model.*, **103** (2022), 674–695. https://doi.org/10.1016/j.apm.2021.11.012
17. L. Yang, O. Harrysson, H. West, D. Cormier, Mechanical properties of 3d re-entrant honeycomb auxetic structures realized via additive manufacturing, *Int. J. Solids Struct.*, **69-70** (2015), 475–490. https://doi.org/10.1016/j.ijsolstr.2015.05.005
18. C. Liu, Y. Wang, W. Zhang, K. Yu, J. J. Mao, H. Shen, Nonlinear dynamics of a magnetic vibration isolator with higher-order stable quasi-zero-stiffness, *Mech. Syst. Signal Process.*, **218** (2024), 111584–111607. https://doi.org/10.1016/j.ymssp.2024.111584
19. Q. Zhu, K. Chai, Magnetic negative stiffness devices for vibration isolation systems: A state-of-the-art review from theoretical models to engineering applications, *Appl. Sci.*, **14** (2024), 4698–4739. https://doi.org/10.3390/app14114698
20. J. Yang, D. Ning, S. S. Sun, J. Zheng, H. Lu, M. Nakano, et al., A semi-active suspension using a magnetorheological damper with nonlinear negative-stiffness component, *Mech. Syst. Signal Process.*, **147** (2021), 107071–107091. https://doi.org/10.1016/j.ymssp.2020.107071
21. T. Zhu, B. Cazzolato, W. S. P. Robertson, A. Zander, Vibration isolation using six degree-of-freedom quasi-zero stiffness magnetic levitation, *J. Sound Vib.*, **358** (2015), 48–73. https://doi.org/10.1016/j.jsv.2015.07.013
22. M. H. Moghadam, M. R. Zakerzadeh, M. Ayati, Development of a cascade position control system for an sma-actuated rotary actuator with improved experimental tracking results, *J. Braz. Soc. Mech. Sci. Eng.*, **41** (2019), 407–420. https://doi.org/10.1007/s40430-019-1896-3
23. E. Rustighi, M. J. Brennan, B. R. Mace, A shape memory alloy adaptive tuned vibration absorber: Design and implementation, *Smart Mater. Struct.*, **14** (2005), 19–28. https://doi.org/10.1088/0964-1726/14/1/002
24. H. Du, X. He, L. Wang, R. Melnik, Analysis of shape memory alloy vibrator using harmonic balance method, *Appl. Phys. A*, **126** (2020), 568–577. https://doi.org/10.1007/s00339-020-03740-x
25. G. Song, N. Ma, H. N. Li, Applications of shape memory alloys in civil structures, *Eng. Struct.*, **28** (2006), 1266–1274. https://doi.org/10.1016/j.engstruct.2005.12.010

26. F. A. dos Santos, J. Nunes, Toward an adaptive vibration absorber using shape-memory alloys, for civil engineering applications, *J. Intell. Mater. Syst. Struct.*, **29** (2017), 729–740. https://doi.org/10.1177/1045389x17721031
27. L. Wang, R. Melnik, Simulation of phase combinations in shape memory alloys patches by hybrid optimization methods, *Appl. Numer. Math.*, **58** (2008), 511–524. https://doi.org/10.1016/j.apnum.2007.01.013
28. L. Wang, R. Melnik, Dynamics of shape memory alloys patches with mechanically induced transformations, *Discrete Contin. Dyn. Syst.*, **15** (2006), 1237–1252. https://doi.org/10.3934/dcds.2006.15.1237
29. D. C. Lagoudas, *Shape Memory Alloys*, Springer Nature, 2008. https://doi.org/10.1007/978-0-387-47685-8
30. C. Maletta, A. Falvo, F. Furgiuele, A phenomenological approach for real-time simulation of the two-way shape memory effect in niti alloys, *J. Eng. Mater. Technol.*, **130** (2008), 011003–011012. https://doi.org/10.1115/1.2806264
31. C. Maletta, A. Falvo, F. Furgiuele, J. N. Reddy, A phenomenological model for superelasticity in niti alloys, *Smart Mater. Struct.*, **18** (2009), 025005–025014. https://doi.org/10.1088/0964-1726/18/2/025005
32. J. S. Shaw, C. A. Wang, Design and control of adaptive vibration absorber for multimode structure, *J. Intell. Mater. Syst. Struct.*, **30** (2019), 1043–1052. https://doi.org/10.1177/1045389x19828831
33. Z. Lu, K. Rong, L. Tian, C. Qiu, J. Du, Studies on the damping mechanism of shape memory alloy-spring tuned vibration absorber attached to a multi-degree-of-freedom structure, *J. Vib. Control*, **28** (2021), 2666–2677. https://doi.org/10.1177/10775463211018526
34. L. Wang, M. Willatzen, Extension of the landau theory for hysteretic electric dynamics in ferroelectric ceramics, *J. Electroceram.*, **24** (2010), 51–57. https://doi.org/10.1007/s10832-008-9525-z
35. F. Wang, H. Y. Du, L. X. Wang, A modified landau phenomenological constitutive model for the tension–compression asymmetry in one-dimensional shape memory alloys, *Mech. Mater.*, **156** (2021), 103795. https://doi.org/10.1016/j.mechmat.2021.103795
36. L. Wang, R. V. N. Melnik, Nonlinear dynamics of shape memory alloy oscillators in tuning structural vibration frequencies, *Mechatronics*, **22** (2012), 1085–1096. https://doi.org/10.1016/j.mechatronics.2012.09.004
37. L. X. Wang, R. V. N. Melnik, Numerical model for vibration damping resulting from the first-order phase transformations, *Appl. Math. Modell.*, **31** (2007), 2008–2018. https://doi.org/10.1016/j.apm.2006.08.019
38. V. I. Arnol'd, *Mathematical Methods of Classical Mechanics*, Springer Science & Business Media, 2013. https://doi.org/10.1007/978-1-4757-2063-1
39. L. Wang, R. V. N. Melnik, Control of coupled hysteretic dynamics of ferroelectric materials with a landau-type differential model and feedback linearization, *Smart Mater. Struct.*, **18** (2009), 074011. https://doi.org/10.1088/0964-1726/18/7/074011
40. J. C. Lagarias, J. A. Reeds, M. H. Wright, P. E. Wright, Convergence properties of the Nelder-Mead simplex method in low dimensions, *SIAM J. Optim.*, **9** (1998), 112–147. https://doi.org/0.1137/S1052623496303470

41. S. L. Lau, Y. K. Cheung, S. Y. Wu, Incremental harmonic balance method with multiple time scales for aperiodic vibration of nonlinear systems, *J. Appl. Mech.*, **50** (1983), 871–876. https://doi.org/10.1115/1.3167160



AIMS Press

©2025 the Author(s), licensee AIMS Press. This is an open access article distributed under the terms of the Creative Commons Attribution License (https://creativecommons.org/licenses/by/4.0)